

# A Majority of Solar Wind Intervals Support Ion-Driven Instabilities

K. G. Klein,<sup>1,2,\*</sup> B. L. Alterman,<sup>1</sup> M. L. Stevens,<sup>3</sup> D. Vech,<sup>1</sup> and J. C. Kasper<sup>1,3</sup>

<sup>1</sup>*Climate and Space Sciences and Engineering, University of Michigan, Ann Arbor, MI 48109, USA*

<sup>2</sup>*Lunar and Planetary Laboratory, University of Arizona, Tucson, AZ 85719, USA*

<sup>3</sup>*Smithsonian Astrophysical Observatory, Cambridge, MA 02138 USA*

(Dated: May 2, 2018)

We perform a statistical assessment of solar wind stability at 1 AU against ion sources of free energy using Nyquist’s instability criterion. In contrast to typically employed threshold models which consider a single free-energy source, this method includes the effects of proton and  $\text{He}^{2+}$  temperature anisotropy with respect to the background magnetic field as well as relative drifts between the proton core, proton beam, and  $\text{He}^{2+}$  components on stability. Of 309 randomly selected spectra from the Wind spacecraft, 53.7% are unstable when the ion components are modeled as drifting bi-Maxwellians; only 4.5% of the spectra are unstable to long-wavelength instabilities. A majority of the instabilities occur for spectra where a proton beam is resolved. Nearly all observed instabilities have growth rates  $\gamma$  slower than instrumental and ion-kinetic-scale timescales. Unstable spectra are associated with relatively-large  $\text{He}^{2+}$  drift speeds and/or a departure of the core proton temperature from isotropy; other parametric dependencies of unstable spectra are also identified.

*Introduction.*— Plasma instabilities, wave-particle interactions driven by departures from local thermodynamic equilibrium, influence the dynamics of nearly collisionless systems, including those frequently encountered in space and astrophysical contexts. In order to transfer free energy from plasma particles to electromagnetic fields and drive unstable growth, non-equilibrium attributes— including anisotropic temperatures relative to the local mean magnetic field, relative drifts between component distributions, and more general agyrotropic features— must either contribute to sufficiently large departures from equilibrium or enable a resonant interaction between fields and velocity-space structure in the particle distribution. The determination of these conditions is complicated in systems with many sources of free energy.

The large number of in situ observations of the solar wind, a nearly-collisionless, low-density, high-temperature plasma emanating from the Sun’s surface, enables the statistical study of plasma processes, including instabilities. Typical instability studies focus on what unstable modes may arise due to a single free-energy source in a reduced parameter space. As an example, the departure of the proton temperature ratio  $T_{\perp p}/T_{\parallel p}$  from isotropy, where  $\perp$  and  $\parallel$  are defined with respect to the mean magnetic field  $\mathbf{B}$ , can drive Alfvén ion cyclotron[1, 2], mirror[3–5], parallel firehose[6, 7], Alfvén (or oblique) firehose[8], or CGL (or long-wavelength) firehose[9] instabilities. Similar instabilities arise for electron and minor ion temperature anisotropies, and other instabilities arise due to drifts between the distributions. A recent review of kinetic plasma instabilities can be found in Yoon 2017[10].

For each kind of unstable mode, one can determine using linear theory the threshold value of a single parameter, assuming all other plasma parameters are held constant, beyond which the fastest growing mode has a

growth rate exceeding some specified value  $\gamma_{\min}$ . Varying a second parameter enables the construction of a stability threshold model for each kind of unstable mode for a single free-energy source[11, 12]. Such models must be modified for any variation of other plasma parameters, including minor ion densities or relative drifts between components, which can suppress or enhance the modeled instability as well as drive other unstable modes[13–15].

These simple two-parameter models were combined with decades of observations to demonstrate that the solar wind’s evolution is bound by long-wavelength instabilities, specifically by the mirror and CGL firehose thresholds[16–18]. Chen et al. 2016 [19] accounted for the free energy contribution from protons, electrons, and  $\text{He}^{2+}$  ( $\alpha$ ) to long-wavelength instability thresholds, further demonstrating that the solar wind is well constrained by these long-wavelength instabilities and that each plasma species contributes to the stability threshold. However, such long-wavelength thresholds neglect instabilities arising at kinetic scales, and in the case of the mirror mode threshold, neglect the effects of relatively drifting components. Using these methods, the majority of intervals were found to be stable, with only a few percent classified as unstable.

Instead of focusing on a single free-energy source or using long-wavelength thresholds which neglect kinetic-scale instabilities, we identify the presence of any ion-driven instabilities using a numerical implementation of Nyquist’s instability criterion[20, 21], which determines the number of unstable modes supported by a specified linearized equilibrium via a contour integral. Of a statistically random set of Wind observations with protons and alpha particles modeled as a collection of drifting bi-Maxwellians, 53.7% are found to be unstable. Unstable modes preferentially arise at parallel ion-kinetic scales and for spectra with an observed proton beam. Instabilities appear to be pervasive in the solar wind, rather

than simply serving as a boundary that constrains its evolution, only acting on a minority of intervals.

*Nyquist’s Instability Criterion.*— Nyquist’s method determines if any complex frequency solutions  $[\omega, \gamma](\mathbf{k})$  to a dispersion relation  $|D(\omega, \gamma, \mathbf{k}, \mathcal{P})| = 0$  have a positive imaginary component  $\gamma > 0$  and thus are unstable for a given wavevector  $\mathbf{k}$  and other system parameters  $\mathcal{P}$ [20]. This is achieved by calculating the contour integral of  $|D|^{-1}$  over the upper half of the complex frequency plane for fixed values of  $\mathbf{k}$  and  $\mathcal{P}$  and counting the number of enclosed poles via the residue theorem, producing an integer the winding number  $W_n$ . If  $W_n = 0$ , the system is stable; if  $W_n = N$ , the system supports  $N$  unstable modes. This method, as well as the specific numerical implementation employed in this work, are described in more detail in Klein et al. 2017[21]. This method does not report the kind of mode driven unstable, only if an unstable mode exists. This calculation can be performed not just to test for absolute instability, integrating over the complex half-plane with lower boundary  $\gamma = 0$ , but for any minimum growth rate, performing a contour integral with arbitrary lower boundary  $\gamma = \gamma_{\min}$ , yielding the number of unstable modes with growth rates larger than  $\gamma_{\min}$ ,  $W_n(\mathbf{k}, \mathcal{P}, \gamma_{\min})$ .

To apply Nyquist’s method to solar wind observations, we treat the solar wind as a hot, magnetized plasma consisting of a collection of drifting bi-Maxwellian populations. The linear response of this system is described by the set of parameters  $\mathcal{P}$  which includes a normalized density  $n_s/n_{\text{ref}}$ , drift speed relative to the reference distribution  $v_s$  normalized by the Alfvén speed  $v_A = B/\sqrt{4\pi n_{\text{ref}} m_{\text{ref}}}$ , parallel and perpendicular temperatures defined by  $T_{\perp s}/T_{\parallel s}$  and  $T_{\parallel s}/T_{\parallel \text{ref}}$ , charge  $q_s/q_{\text{ref}}$  and mass  $m_s/m_{\text{ref}}$  for each component  $s$ , as well as a reference plasma beta  $\beta_{\parallel \text{ref}} = 8\pi n_{\text{ref}} T_{\parallel \text{ref}}/B^2$  and thermal speed  $v_{\text{tref}}/c = \sqrt{2T_{\parallel \text{ref}}/m_{\text{ref}}c^2}$ . The linear dispersion relation  $|D|$  for such a system is calculated as a function of wavevector  $(k_{\perp}, k_{\parallel})\rho_{\text{ref}}$  normalized to the reference gyroradius  $\rho_{\text{ref}} = v_{\text{tref}}/\Omega_{\text{ref}}$  using the PLUME numerical solver[22]. We calculate  $W_n(\mathbf{k}, \mathcal{P}, \gamma_{\min})$  by numerical integration of  $|D|^{-1}$  using the proton core distribution as the reference species and normalizing our time scales by the proton gyrofrequency  $\Omega_p = q_p B/m_p c$ . For an observed  $\mathcal{P}$ , we calculate  $W_n(\mathbf{k}, \mathcal{P}, \gamma_{\min})$  over a log-spaced grid covering  $(k_{\perp}, k_{\parallel})\rho_p \in [10^{-2}, 10^1]$  and define the unstable mode density as  $\delta(\gamma_{\min}) = [\int d\mathbf{k} W_n(\mathbf{k}, \mathcal{P}, \gamma_{\min})] / \int d\mathbf{k}$ .

*Data.*—We choose for our analysis a random set of solar wind observations, rather than intervals associated with signatures for the presence of instabilities[23], selecting the first nominal peak-tracking mode spectrum of the day measured by the Solar Wind Experiment Faraday cup [24] on the Wind spacecraft from 309 days in 2016 and 2017; data from the magnetometer[25, 26] is used to determine the orientation and amplitude of the

	# Spectra	# Unstable	Mirror	CGL FH	Kinetic
Total	309	166	14	1	151
p, b, & $\alpha$	189	130	12	0	118
p & $\alpha$	114	33	2	1	30
p & b	5	3	0	0	3
p	1	0	0	0	0

TABLE I. Total number, and number of unstable, spectra. The results are divided between cases with and without resolved proton beam and/or  $\alpha$  components. The unstable spectra are further divided into mirror, CGL firehose, and ion-kinetic-scale instabilities.

magnetic field. For each spectrum, a nonlinear-least-squares Bi-Maxwellian fit is performed for up to three ion components— a proton core, proton beam, and  $\alpha$  population— using intelligent initial guesses to find the simplest physical model that fits the data. The number of spectra with resolved proton beams and/or an  $\alpha$  population is listed in Table I. While inclusion of electron free-energy sources may decrease stability at fluid and kinetic scales [19, 27], the details of the electron VDF will not significantly inhibit ion-driven instabilities. We treat the electrons as isotropic Maxwellians with  $T_e = T_p = (2T_{\perp p} + T_{\parallel p})/3$  and a drift speed necessary to ensure zero net current.

For spectra without a proton beam population, values for 7 dimensionless parameters are extracted from Bi-Maxwellian fits:  $\beta_{\parallel p}$ ,  $v_{tp}/c$ ,  $T_{\perp p}/T_{\parallel p}$ ,  $T_{\perp \alpha}/T_{\parallel \alpha}$ ,  $T_{\parallel \alpha}/T_{\parallel p}$ ,  $n_{\alpha}/n_p$ , and  $v_{\alpha}/v_A$ . For spectra with a proton beam, 4 additional parameters are used:  $T_{\perp b}/T_{\parallel b}$ ,  $T_{\parallel b}/T_{\parallel p}$ ,  $n_b/n_p$ , and  $v_b/v_A$ . Mean values of these parameters, given in Table II, are consistent with previous statistical studies of solar wind observations[28], though the inclusion of proton beams in this work reduces  $T_{\parallel p}$  compared to studies which assume a single proton population. We calculate  $W_n(\mathbf{k}\rho_p, \mathcal{P}, \gamma_{\min} = 0)$  as a function of  $(k_{\perp}, k_{\parallel})\rho_p$ ; example winding number distributions and unstable mode densities  $\delta$  for three unstable spectra are shown in Fig. 1, as well as the mean winding number  $\overline{W}_n(\mathbf{k}\rho_p, \gamma_{\min} = 0)$  averaged over all 309 spectra.

*Occurrence of Instability*— We find that 53.7% of the randomly selected spectra have  $\delta(\gamma_{\min} = 0) > 0$  and thus support at least one growing mode in  $(k_{\perp}, k_{\parallel})\rho_p \in [10^{-2}, 10^1]$ . Considering the spectra with (without) a proton beam, 70.0% (28.7%) are unstable; a summary of the number of unstable modes as a function of the resolved components is presented in Table I. Fig. 2 illustrates the  $(\beta_{\parallel p}, T_{\perp p}/T_{\parallel p})$  distribution of the 309 spectra; unstable spectra are color-coded by the associated unstable mode density  $\delta$  and stable spectra are plotted in grey. The stability thresholds for proton-temperature anisotropy-driven instabilities with  $\gamma_{\min} = 10^{-3}\Omega_p$ [12] are included for context.

The mean winding number  $\overline{W}_n(\mathbf{k}\rho_p, 0)$ , Fig. 1(c), shows that most unstable modes arise at parallel

	$\beta_{\parallel p}$	$10^4 v_{tp}/c$	$T_{\perp p}/T_{\parallel p}$	$T_{\perp \alpha}/T_{\parallel \alpha}$	$T_{\perp b}/T_{\parallel b}$	$T_{\parallel \alpha}/T_{\parallel p}$	$T_{\parallel b}/T_{\parallel p}$	$n_{\alpha}/n_p$	$n_b/n_p$	$ v_{\alpha} /v_A$	$ v_b /v_A$
Total	0.60	1.07	1.57	0.96	1.48	10.89	2.72	0.04	0.43	0.31	0.84
Stable	0.50	0.91	1.12	1.03	1.39	5.24	2.35	0.04	0.41	0.16	0.73
Unstable	0.68	1.21	1.96	0.90	1.52	15.74	2.88	0.05	0.44	0.44	0.89
$\Delta X_{p,\alpha,b}(\%)$	19.12	13.46	50.59	-21.06	8.45	64.27	20.83	2.61	2.90	61.57	21.84
$\Delta X_{p,\alpha}(\%)$	132.53	57.59	-26.77	14.16	—	26.46	—	18.10	—	77.44	—

TABLE II. Mean plasma parameters for the 309 observed spectra (top row), for the stable and unstable spectra (second and third), and the normalized difference of the parameters  $\Delta X$  between stable and unstable spectra (fourth and fifth).

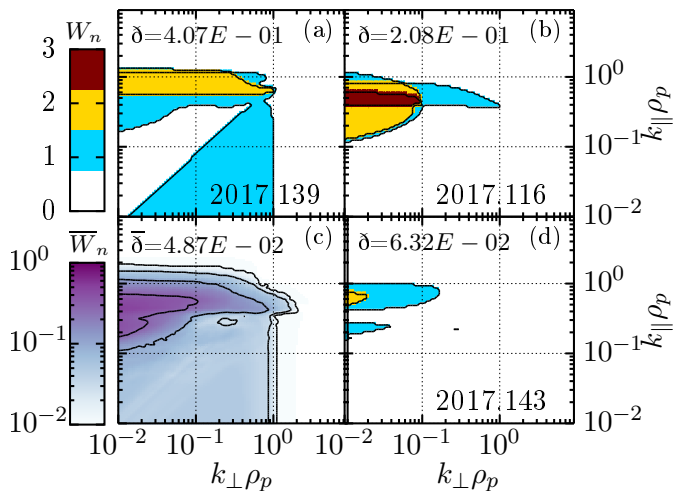


FIG. 1. (a,b,d) The number of unstable modes with  $\gamma_{\min} > 0$  as a function of wavevector  $\mathbf{k}\rho_p$  for three example spectra. (c) The mean winding number averaged over the 309 observed spectra.

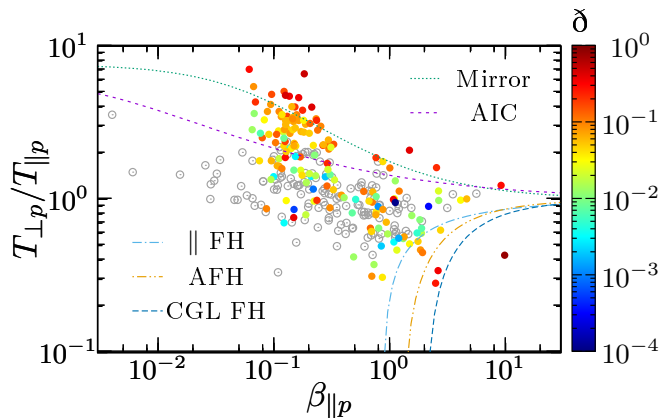


FIG. 2. The  $(\beta_{\parallel p}, T_{\perp p}/T_{\parallel p})$  distribution of the observed spectra; color indicates the unstable mode density  $\delta$ , and grey indicates a stable spectrum.

wavevectors near ion kinetic scales ( $k_{\perp}\rho_p < k_{\parallel}\rho_p \lesssim 1$ ) though there exist a finite number of unstable modes at long wavelengths and/or at more oblique wavevectors. The abrupt cutoff of  $\bar{W}_n$  beyond  $k\rho_p \approx 1$  is due to our model's lack of electron free-energy sources, which are

necessary to drive instabilities between ion and electron kinetic scales.

To determine what kinds of instabilities arise for a given spectrum, we inspect  $W_n(\mathbf{k}\rho_p, \mathcal{P}, 0)$  for the 166 unstable spectra. For the mirror instability, the long-wavelength threshold[29] can not be simply applied, as it does not account for the effects of relative drift between distributions. Instead, we identified 14 spectra that have unstable modes with  $|k\rho_p|$  extending from long-wavelengths up to the proton gyroscale covering oblique angles,  $k_{\perp} > k_{\parallel}$ . These intervals are classified as mirror unstable; an example of such a spectrum is found in Fig. 1(a). For each mirror unstable case, there also exist kinetic instabilities with  $k_{\parallel}\rho_p \lesssim 1$ , in agreement with the canonical  $T_{\perp p}/T_{\parallel p} > 1$  mirror unstable distribution, (e.g. Fig. 2(c) of Klein et al. 2017[21]). One spectrum, not shown, exceeds the long-wavelength CGL firehose threshold[30] and has a winding number distribution similar to the canonical case (e.g. Fig. 2(f) of Klein et al. 2017), driving unstable modes for nearly all wavevectors with  $k\rho_p < 1$ , one (two) mode(s) for  $k_{\perp} > (<)k_{\parallel}$ . We classify the remaining 151 unstable spectra with growing modes satisfying  $k_{\perp}\rho_p < k_{\parallel}\rho_p \lesssim 1$  as kinetic; two example  $W_n$  distributions for these kinetic cases are shown in Fig. 1(b) and (d). The instability classification as a function of resolved ion components is given in Table I.

Using this classification scheme, we repeat our analysis for a range of minimum growth rates  $\gamma_{\min} \in [10^{-4}, 10^0]\Omega_p$ , shown in Fig. 3. We see that (black line in Fig. 3(a)) the fraction of unstable spectra decreases with an increase in  $\gamma_{\min}$ , with no spectrum having growth rates exceeding  $\gamma > 0.2\Omega_p$ . The number of mirror and CGL firehose unstable modes (red and blue regions) remains constant with increasing  $\gamma_{\min}$  up to  $0.1\Omega_p$ . Most of the kinetic instabilities associated with spectra without proton beams (dark grey) are limited to growth rates less than  $10^{-2}\Omega_p$ , while a decreasing fraction of the unstable spectra with proton beams (light grey) persists to  $0.1\Omega_p$ .

*Instability Timescales*— To compare  $\gamma_{\min}$  with timescales other than  $\Omega_p^{-1}$ , we calculate the fraction of unstable spectra as a function of four additional time scales; the advected proton gyroscale timescale  $\rho_p/v_{\text{SW}}$ , the advected proton inertial length timescale  $d_p/v_{\text{SW}} = v_A/(\Omega_p v_{\text{SW}})$ , the Faraday cup measurement period  $\tau_{\text{Wind}} = 92$  s, and  $\tau_{\text{nl}} = (k_0\rho_p)^{-1/3}\rho_p/v_A$ , an es-

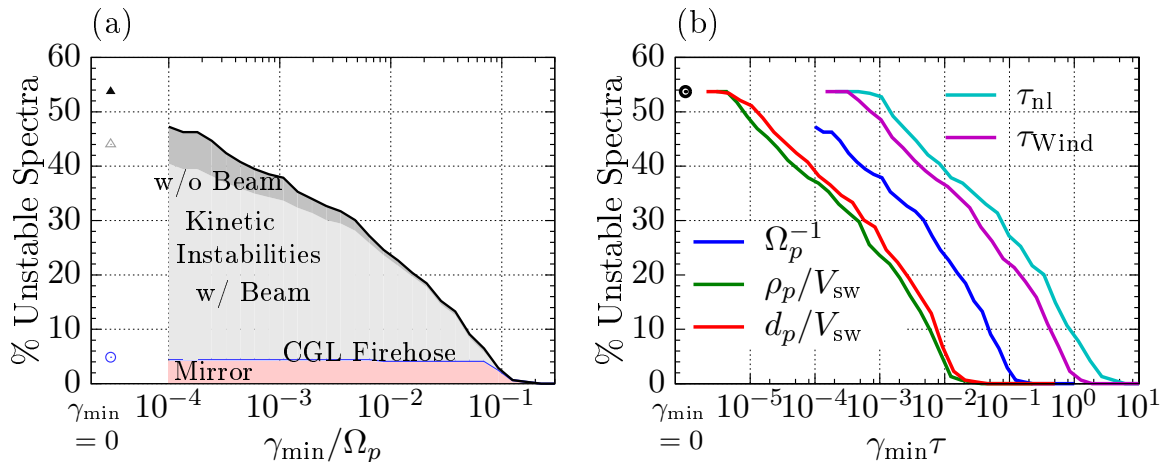


FIG. 3. The fraction of observed spectra supporting unstable modes with growth rate exceeding  $\gamma_{\min}$ . (a) The spectra are divided according to the instability classification presented in the text. (b) The minimum growth rate distribution is re-scaled by selected timescales  $\tau$ .

timate for the nonlinear turbulent energy transfer time at the proton gyroscale  $k_{\perp}\rho_p = 1$  assuming a critically balanced cascade of energy[31, 32] from an outer scale  $k_0\rho_p = 10^{-4}$ . For each spectrum, the values for these timescales are calculated and the unstable mode density  $\delta(\gamma_{\min}/\Omega_p)$  is interpolated onto a log-spaced grid for  $\delta(\gamma_{\min}\tau)$ . This distribution is averaged over the 309 spectra to calculate the fraction of unstable spectra as a function of  $\tau$ , shown in Fig. 3(b).

The unstable modes typically have growth rates slower than ion-kinetic timescales. Nearly all unstable spectra have growth rates slower than a hundredth of  $\rho_p/v_{\text{SW}}$  or  $d_p/v_{\text{SW}}$ , indicating any growing ion-kinetic-scale structure associated with instabilities will be static in the spacecraft frame. As nearly all unstable spectra have growth rates slower than 92s the nominal spectra selected for this work are in steady state with respect to any instability induced evolution. Less than 10% of the spectra have growth rates faster than  $\tau_{\text{nl}}$ , indicating that only a small fraction of the instabilities act quickly enough to compete with ion-scale damping processes.

*Parametric Dependence.*—We wish to determine any relation between a velocity distribution’s bulk parameters and its stability. Given the high-dimensionality of the parameter space —  $3 + 4(N_{\text{ion}} - 1)$  values for  $N_{\text{ion}}$  resolved ion components— it is difficult to determine the relative importance of a given parameter; previous attempts typically focused on the effects of a handful of parameters, e.g.  $\beta_{\parallel p}$  and  $T_{\perp,p}/T_{\parallel,p}$ . To ascertain any relation, we calculate the normalized difference

$$\Delta X \equiv \frac{\bar{X}_{\text{unstable}} - \bar{X}_{\text{stable}}}{\bar{X}_{\text{total}}} \quad (1)$$

with  $X$  drawn from the ion bulk parameters;  $\bar{X}_{\text{total}}$ ,  $\bar{X}_{\text{unstable}}$  and  $\bar{X}_{\text{stable}}$  are the mean value of  $X$  averaged over all spectra, over the unstable spectra, and over the

stable spectra, with stability determined using  $\gamma_{\min} = 0$ . Selection of larger  $\gamma_{\min}/\Omega_p$  does not qualitatively alter these results. We calculate  $\Delta X$  using two disjoint subsets of data; spectra with a resolved alpha distribution and proton core, or spectra with all three ion components resolved. Values of  $\Delta X$  are presented in Table II.

Unstable spectra both without and with proton beams have higher mean alpha drift velocities  $v_{\alpha}/v_A$  than stable spectra, indicating that the free energy associated with the larger relative drift between the protons and alphas is important in driving instabilities. The mean core proton temperature anisotropy  $T_{\perp p}/T_{\parallel p}$  for unstable spectra is significantly decreased (increased) from isotropy for cases without (with) a proton beam. This reduction of temperature anisotropy is potentially due to the beam having relaxed into the proton core, leading to an increased  $T_{\parallel p}$ .

For the no-proton-beam case,  $\beta_{\parallel p}$  is significantly larger for the unstable spectra, with a 132% increase compared to stable spectra. The normalized core proton thermal speed  $v_{tp}/c$ , our dimensionless proxy for the parallel core proton temperature, is also significantly larger. Combined with the normalized difference  $\Delta|v_{\alpha}|/v_A$ , this indicates that parallel free energy is important for driving these systems unstable.

For spectra with proton beams,  $T_{\parallel\alpha}/T_{\parallel p}$  is increased for unstable spectra. The proton beam is also slightly hotter while the alpha temperature anisotropy  $T_{\perp\alpha}/T_{\parallel\alpha}$  is slightly decreased. The values of the other proton beam parameters are only marginally increased for unstable spectra.

*Effects of Uncertainty*— To consider the robustness of this method against measurement uncertainty, we follow Klein et al. 2017[21] and repeat our instability analysis on an ensemble of 100 Monte Carlo variations of  $\mathcal{P}$  for each of the 309 observed spectra. Each observed dimensional quantity from which  $\mathcal{P}$  is composed is replaced by a

Gaussian-distributed random variable with a mean of the original quantity and a standard deviation of 10%. The width of the random variable distribution is motivated by measurement uncertainties found for instance by Kasper et al. 2006[33]. For these 31,209 values of  $\mathcal{P}$ , 56.0% are unstable, qualitatively similar to 53.7% calculated from the observed spectra. For the ensembles corresponding to stable observations,  $\mathcal{P}(\delta_0 = 0)$ , an average of 83.6% of the elements are stable; for  $\mathcal{P}(\delta_0 \neq 0)$ , an average of 90.5% are unstable. Of the  $\delta_0 \neq 0$  ensembles, 0.6% have a majority of their elements stable, while 8.3% of the  $\delta_0 = 0$  ensembles are majority unstable.

In addition to measurement uncertainty, our results may be affected by unresolved proton beams with small  $n_b/n_p$  or  $v_b/v_A$ , or by the assumption of bi-Maxwellian distributions[34, 35]. Repeating this work with a dispersion relation which neglects analytic forms and captures non-Maxwellian features[36] will enable more accurate determination of solar wind stability.

*Conclusions.*—We assess the stability of 309 randomly selected solar wind spectra with ion components modeled as a collection of drifting bi-Maxwellians using Nyquist’s instability criterion and find 53.7% are unstable. This mode-agnostic method includes the effects of ion drifts and temperature anisotropies, contrasting with previously employed threshold models that identify only a small fraction of solar wind intervals as unstable. This method identifies the same instabilities as traditional Vlasov studies, but does not require a priori knowledge of which linear modes are unstable, allowing for automated analysis. The unstable modes identified using Nyquist’s criterion are primarily kinetic, with  $k_\perp \rho_p < k_\parallel \rho_p \lesssim 1$ ; only 4.5% of the observed spectra have long-wavelength instabilities. The maximum growth rate for these unstable modes is slower than measurement and ion-kinetic timescales. The mean alpha drift speed for unstable spectra is larger than for stable spectra, and the ratio  $T_{\perp p}/T_{\parallel p}$  for unstable spectra is further from isotropy. The majority of the unstable spectra have a resolved proton beam component.

Further study is needed to assess the effects of this profusion of instabilities. While a majority of observed spectra are unstable, it remains unclear from this initial study if all the inferred instabilities are dynamically important, or simply a byproduct of other processes. The resonant instabilities which comprise the majority of the unstable spectra do not act as efficiently as long-wavelength instabilities to return the plasma toward isotropy and therefore may not constrain the dynamics of the solar wind’s evolution. This may be an effect of slower growth rates, smaller regions of wavevector space being driven unstable, or departures from the assumed bi-Maxwellian distribution affecting resonance conditions.

One way to discern if these instabilities are continuously generated or a remnant of processes in the near-Sun environment, and how their role in solar wind

dynamics changes at varying distances from the Sun, will be to combine this automated instability detection method with forthcoming measurements from Parker Solar Probe[37] and Solar Orbiter[38].

*Acknowledgments.*— The spectrum data used in this project were taken from the WI\_SW-ION-DIST\_SWE-FARADAY database at [cdaweb.gsfc.nasa.gov](http://cdaweb.gsfc.nasa.gov). The authors would like to acknowledge inspiring conversations with Alfred Mallet. This work was supported by NASA grant NNX14AR78G, with K.G. Klein receiving additional support from NASA grant NNX16AG81G.

---

\* [kgklein@email.arizona.edu](mailto:kgklein@email.arizona.edu)

- [1] C. F. Kennel and H. E. Petschek, *J. Geophys. Res.* **71**, 1 (1966).
- [2] R. C. Davidson and J. M. Ogden, *Physics of Fluids* **18**, 1045 (1975).
- [3] M. Tajiri, *Journal of the Physical Society of Japan* **22**, 1482 (1967).
- [4] D. J. Southwood and M. G. Kivelson, *J. Geophys. Res.* **98**, 9181 (1993).
- [5] M. G. Kivelson and D. J. Southwood, *J. Geophys. Res.* **101**, 17365 (1996).
- [6] K. B. Quest and V. D. Shapiro, *J. Geophys. Res.* **101**, 24457 (1996).
- [7] S. P. Gary, H. Li, S. O’Rourke, and D. Winske, *J. Geophys. Res.* **103**, 14567 (1998).
- [8] P. Hellinger and H. Matsumoto, *J. Geophys. Res.* **105**, 10519 (2000).
- [9] G. F. Chew, M. L. Goldberger, and F. E. Low, *Royal Society of London Proceedings Series A* **236**, 112 (1956).
- [10] P. H. Yoon, *Reviews of Modern Plasma Physics* **1**, 4 (2017).
- [11] P. Hellinger, P. Trávníček, J. C. Kasper, and A. J. Lazarus, *Geophys. Res. Lett.* **33**, L09101 (2006).
- [12] D. Verscharen, B. D. G. Chandran, K. G. Klein, and E. Quataert, *Astrophys. J.* **831**, 128 (2016), [arXiv:1605.07143 \[physics.space-ph\]](https://arxiv.org/abs/1605.07143).
- [13] C. P. Price, D. W. Swift, and L.-C. Lee, *J. Geophys. Res.* **91**, 101 (1986).
- [14] J. J. Podesta and S. P. Gary, *Astrophys. J.* **742**, 41 (2011).
- [15] B. A. Maruca, J. C. Kasper, and S. P. Gary, *Astrophys. J.* **748**, 137 (2012).
- [16] J. C. Kasper, A. J. Lazarus, and S. P. Gary, *Geophys. Res. Lett.* **29**, 1839 (2002).
- [17] L. Matteini, S. Landi, P. Hellinger, F. Pantellini, M. Maksimovic, M. Velli, B. E. Goldstein, and E. Marsch, *Geophys. Res. Lett.* **34**, L20105 (2007).
- [18] S. D. Bale, J. C. Kasper, G. G. Howes, E. Quataert, C. Salem, and D. Sundkvist, *Phys. Rev. Lett.* **103**, 211101 (2009), [arXiv:0908.1274 \[astro-ph.SR\]](https://arxiv.org/abs/0908.1274).
- [19] C. H. K. Chen, L. Matteini, A. A. Schekochihin, M. L. Stevens, C. S. Salem, B. A. Maruca, M. W. Kunz, and S. D. Bale, *Astrophys. J. Lett.* **825**, L26 (2016), [arXiv:1606.02624 \[physics.space-ph\]](https://arxiv.org/abs/1606.02624).
- [20] H. Nyquist, *Bell system technical journal* **11**, 126 (1932).
- [21] K. G. Klein, J. C. Kasper, K. E. Korreck, and M. L.

- Stevens, J. *Geophys. Res.*, 9815 (2017), 2017JA024486.
- [22] K. G. Klein and G. G. Howes, *Phys. Plasmas* **22**, 032903 (2015), arXiv:1503.00695 [physics.space-ph].
- [23] S. P. Gary, L. K. Jian, T. W. Broiles, M. L. Stevens, J. J. Podesta, and J. C. Kasper, *J. Geophys. Res.* **121**, 30 (2016).
- [24] K. W. Ogilvie, D. J. Chornay, R. J. Fritzenreiter, F. Hunsaker, J. Keller, J. Lobell, G. Miller, J. D. Scudder, E. C. Sittler, Jr., R. B. Torbert, D. Bodet, G. Needell, A. J. Lazarus, J. T. Steinberg, J. H. Tappan, A. Mavretic, and E. Gergin, *Space Sci. Rev.* **71**, 55 (1995).
- [25] R. P. Lepping, M. H. Acuña, L. F. Burlaga, W. M. Farrell, J. A. Slavin, K. H. Schatten, F. Mariani, N. F. Ness, F. M. Neubauer, Y. C. Whang, J. B. Byrnes, R. S. Kennon, P. V. Panetta, J. Scheifele, and E. M. Worley, *Space Sci. Rev.* **71**, 207 (1995), 10.1007/BF00751330.
- [26] A. Koval and A. Szabo, *Solar Wind 13* **1539**, 211 (2013).
- [27] M. W. Kunz, I. G. Abel, K. G. Klein, and A. A. Schekochihin, ArXiv e-prints (2017), arXiv:1712.02269 [astro-ph.HE].
- [28] L. B. Wilson, III, M. L. Stevens, J. C. Kasper, K. G. Klein, B. A. Maruca, S. D. Bale, T. A. Bowen, M. P. Pulupa, and C. S. Salem, ArXiv e-prints (2018), arXiv:1802.08585 [physics.plasm-ph].
- [29] P. Hellinger, *Phys. Plasmas* **14**, 082105 (2007).
- [30] M. W. Kunz, A. A. Schekochihin, C. H. K. Chen, I. G. Abel, and S. C. Cowley, *J. Plasma Phys.* **81**, 325810501 (2015), arXiv:1501.06771 [astro-ph.HE].
- [31] P. Goldreich and S. Sridhar, *Astrophys. J.* **438**, 763 (1995).
- [32] A. Mallet, A. A. Schekochihin, and B. D. G. Chandran, *Mon. Not. Roy. Astron. Soc.* **449**, L77 (2015), arXiv:1406.5658 [astro-ph.SR].
- [33] J. C. Kasper, A. J. Lazarus, J. T. Steinberg, K. W. Ogilvie, and A. Szabo, *Journal of Geophysical Research (Space Physics)* **111**, A03105 (2006).
- [34] C. T. Dum, E. Marsch, and W. Pilipp, *J. Plasma Phys.* **23**, 91 (1980).
- [35] P. A. Isenberg, *Phys. Plasmas* **19**, 032116 (2012), arXiv:1203.1938 [physics.plasm-ph].
- [36] D. Verscharen, K. G. Klein, B. D. G. Chandran, M. L. Stevens, C. S. Salem, and S. D. Bale, *J. Plasma Phys.* (under review).
- [37] N. J. Fox, M. C. Velli, S. D. Bale, R. Decker, A. Driesman, R. A. Howard, J. C. Kasper, J. Kinnison, M. Kusterer, D. Lario, M. K. Lockwood, D. J. McComas, N. E. Raouafi, and A. Szabo, *Space Sci. Rev.* **204**, 7 (2016).
- [38] D. Müller, R. G. Marsden, O. C. St. Cyr, and H. R. Gilbert, *Sol. Phys.* **285**, 25 (2013), arXiv:1207.4579 [astro-ph.SR].